*Article*

Surface Functionalization Utilizing Mesoporous Silica Nanoparticles for Enhanced Evanescent-Field Mid-Infrared Waveguide Gas Sensing

Diana Al Husseini [1], Yashaswini Karanth [1], Junchao Zhou [2], Daniel Willhelm [1], Xiaofeng Qian [1], Ricardo Gutierrez-Osuna [3], Gerard L. Coté [4], Pao Tai Lin [1,2,*] and Svetlana A. Sukhishvili [1,*]

[1] Department of Materials Science and Engineering, Texas A&M University, College Station, TX 77843, USA; dianaalhusseini1@tamu.edu (D.A.H.); ykaranth@asu.edu (Y.K.); willhelmd@tamu.edu (D.W.); feng@tamu.edu (X.Q.)

[2] Department of Electrical and Computer Engineering, Texas A&M University, College Station, TX 77843, USA; junchao.zhou@tamu.edu

[3] Department of Computer Science and Engineering, Texas A&M University, College Station, TX 77843, USA; rgutier@cse.tamu.edu

[4] Department of Biomedical Engineering, Texas A&M University, College Station, TX 77843, USA; gcote@tamu.edu

* Correspondence: paolin@ece.tamu.edu (P.T.L.); svetlana@tamu.edu (S.A.S.)

Abstract: This work focuses on the development of nanoparticle-based layer-by-layer (LbL) coatings for enhancing the detection sensitivity and selectivity of volatile organic compounds (VOCs) using on-chip mid-infrared (MIR) waveguides (WGs). First, we demonstrate construction of conformal coatings of polymer/mesoporous silica nanoparticles (MSNs) on the surface of Si-based WGs using the LbL technique and evaluate the coating deposition conditions, such as pH and substrate withdrawal speed, on the thickness and homogeneity of the assemblies. We then use the modified WGs to achieve enhanced sensitivity and selectivity of polar organic compounds, such as ethanol, versus non-polar ones, such as methane, in the MIR region. In addition, using density functional theory calculations, we show that such an improvement in sensing performance is achieved due to preferential adsorption of ethanol molecules within MSNs in the vicinity of the WG evanescent field.

Keywords: layer-by-layer; mesoporous silica nanoparticles; nanocoatings; mid-infrared gas sensing

1. Introduction

Mid-infrared (MIR) spectroscopy can achieve high selectivity waveguide (WG)-based devices for gas sensing by measuring absorption at the characteristic vibrational frequencies of different analytes [1,2]. This ability is advantageous for MIR on-chip small form factor optical sensors when compared to other gas sensing techniques, such as high selectivity but larger form factor in gas chromatography mass spectroscopy (GC–MS) systems [3,4] or a smaller form factor but lower selectivity in metal-oxide semiconductor (MOS) [5–7] and electrochemical sensors [8]. The past decade has seen an increased focus on miniaturization of the conventional bench top MIR instrumentation toward enabling on-chip waveguide detection in order to achieve high selectivity and sensitivity in small form factor portable devices [9,10].

However, achieving high sensitivity while preserving selectivity is challenging for on-chip MIR gas sensing. In our prior work, MIR detection sensitivity remained low when bare, unmodified Si-based on-chip WGs were brought in contact with gaseous analytes [11]. This is due to the intrinsically low concentration of analyte molecules in the vapor phase and the limited overlap between the MIR evanescent field (EF) from the on-chip waveguide and the environment. One way to enhance detection sensitivity is to use WG materials with lower refractive indices than Si (such as Si_3N_4) to create a larger overlap between

the EF and the surrounding environment [12,13]. However, this approach generally only leads to limited improvements in sensitivity. Another approach is to use coatings to concentrate gas molecules within the EF of a WG. Thin organic/polymeric coatings have been mostly implemented in the conventional MIR bench top approach for capturing analytes from fluids [14–17]. Yet, very few other studies with organic coatings have been used for detecting gaseous analytes, since they typically fall short due to their poor ability to concentrate gas molecules close to EF. In one successful example, detection of CO_2 gas was facilitated by its reaction with amine groups in the tetraethylenepentamine coatings [18,19]. However, the use of organic/polymeric coatings to detect gases other than CO_2, such as volatile organic compounds (VOCs), remains challenging because organic coatings have similar functional groups to those in VOCs resulting in a spectral overlap. In our recent work, we developed submicron all-nanoparticle coatings for MIR on-chip detection of acetone vapors [20]. The use of inorganic particles rather than polymers in the coating was a promising solution because it overcame the previous shortcomings by having a wide MIR range transparency and a high surface area to volume ratio enabling the concentration of gaseous biomarkers at the vicinity of the EF [20,21]. The coating deposition was enabled by the layer-by-layer (LbL) technique, which provided good substrate adhesion and precise control over film thickness and composition as compared to other coating techniques such as drop-casting, spin-coating and spray-coating [22–24].

In this study, we aim to further develop this strategy by employing a new coating of highly porous, well defined, mesoporous silica nanoparticles (MSNs) to concentrate gas molecules in the vicinity of Si WGs for enhanced detection sensitivity. This strategy offers an added advantage of providing polarity of the surface silanol groups of MSNs that selectively adsorb and concentrate polar gas molecules. Similar silica-based materials were previously explored as coating components to create functional coatings for gas sensing using quartz crystal microbalance (QCM), fiber-optics, ultraviolet-visible spectroscopy, photoluminescence, refractometry and electrical detection [25–30]. However, to our knowledge, LbL assemblies of MSNs for MIR on-chip gas sensing applications have not been explored. This work is also distinct from other WG-based technology used for super resolution imaging, optical filtering and telecommunications [31–33]. Thus, this paper illustrates the advantages of using the LbL technique for a specific polymer/nanoparticle submicron coating system composed of branched polyethylenimine/mesoporous silica nanoparticles (BPEI/MSNs). The developed coatings were then subjected to calcination to remove BPEI for improved transparency in the MIR region. The effect of solution pH and substrate withdrawal speed on coating quality, morphology and thickness is thoroughly characterized in order to optimize surface coverage with mesoporous particles. Finally, the deposited all-inorganic MSN coatings were applied to Si waveguides to explore their ability to provide sensitivity and selectivity enhancement in detecting ethanol vapors versus methane gas.

2. Materials and Methods

2.1. MSNs Synthesis and Characterization

2.1.1. MSNs Synthesis

High purity cetrimonium bromide (CTAB, $CH_3(CH_3)_{15}N(Br)(CH_3)_3$) and ammonia solution ($NH_4OH$, 28–30%) were purchased from VWR International Co. (Radnor, PA, USA). Tetraethylorthosilicate (TEOS, 99.99%), pluronic F-127, branched polyethyleneimine (BPEI, M_w 750 kDa) and ethanol were received from Sigma Aldrich Chemicals Co. (St. Louis, MO, USA). Ultrapure Milli-Q water, deionized (DI), (MilliporeSigma Co., Burlington, MA, USA) with a resistivity of 18.2 MΩ-cm was used in all experiments. All materials were used without further purification. Silicon (Si) wafers (100 orientation, P/B doped) were purchased from WaferPro Inc. (Santa Clara, CA, USA). Before use, wafers were precleaned using ultraviolet (UV) light and concentrated sulfuric acid to remove organic contaminants. The pH of the deposition solutions was adjusted using diluted concentrations of hydrochloric acid (HCl) and sodium hydroxide (NaOH).

MSNs were synthesized using the modified Stöber method [34]. In brief, MSNs were prepared as follows: 0.5 g of CTAB and 2.05 g of F-127 were dissolved in a mixture of 96.0 mL of DI water, 43.0 mL of ethanol and 11.2 mL of ammonia solution by stirring at room temperature. After the dissolution was completed, 1.9 mL of TEOS was added in one shot. The mixture was then stirred for 1 min at 1000 RPM and left undisturbed for 24 h at room temperature to allow silica condensation and formation of the mesoporous network. The white precipitate formed after 24 h was then recovered and washed with DI water twice via centrifugation (14,000 RPM) at room temperature (HERMLE Z 216 MK, Gosheim, Germany). Finally, the collected precipitate was dried at 343 K for at least 12 h. The resulting powder was grinded in a ceramic mortar, and calcinated for 5 h at 823 K in air.

2.1.2. MSNs Characterization

The morphology of MSNs was identified using transmission electron microscopy (TEM, JEOL1200 EX at 100 kV, JEOL USA Inc., Peabody, MA, USA). The samples were prepared by casting a drop of a MSN aqueous solution (0.2 wt.%, pH = 9) on copper square grids (EMS 400-CU, VWR International Co., Radnor, PA, USA). Excess solution was then removed with a filter paper, and the samples were dried at room temperature for at least 12 h before imaging. The ImageJ open source software (imagej.net, ImageJ 1.52a) was used to determine diameters of 200 nanoparticles. Hydrodynamic diameters of MSNs were measured by dynamic light scattering (DLS) (Zetasizer Nano ZS, Westborough, MA, USA). In addition, a zeta potential analyzer, included in the Zetasizer Nano ZS, was used to measure zeta potential of MSNs using electrophoretic light scattering. To that end, 0.2 wt.% aqueous solutions of MSNs at pH 7, 8 and 9 were injected in folded capillary zeta cell cuvettes to perform hydrodynamic diameter and zeta potential measurements. Powder X-ray diffraction (XRD) measurements of the synthesized MSNs were performed using a Bruker D8 da Vinci instrument (Madison, WI, USA) fitted with a Cu source and a LynxEye XE detector (Madison, WI, USA) in Bragg–Brentano (theta-theta mode). Surface area and pore size of MSNs were determined via Brunauer–Emmett–Teller (BET) method [35] based upon nitrogen (N_2) adsorption isotherm. The N_2 isotherm was collected at 77 K on a Micromeritics ASAP 2420 instrument (Micromeritic Instrument Corp., Norcross, GA, USA). Prior to the N_2 adsorption and desorption measurements, the MSN powder sample was activated at 120 °C for 10 h under high vacuum (<100 µbar).

2.2. BPEI/MSN Coating Assembly and Characterization

2.2.1. BPEI/MSN Coating Assembly

Coating assembly deposition was performed on regular crystalline Si (111) substrates. The coatings were assembled using the LbL technique under controlled and conventional dipping conditions. The Si substrates were first immersed in a 0.2 mg/mL BPEI solution of selected pH (7, 8 or 9) for 7 min of equilibration time before substrate withdrawal. This first step was followed by thorough rinsing in DI water. Then, these substrates were immersed in 0.2 wt.% MSN aqueous solution of selected pH (7, 8 or 9) for 7 min and thoroughly rinsed. This four-step dipping process represents one bilayer (BL) deposition. To explore the effect of pH on coating deposition, all the dipping solutions and DI water used for rinsing were kept at the same pH (7, 8 or 9). For controlled substrate withdrawal, the substrate withdrawal speed was varied at 0.001, 0.01, 0.1 and 1 cm/s. For comparison purposes, a conventional dipping technique was also performed, where the substrates were withdrawn manually in a fast and uncontrolled manner.

2.2.2. BPEI/MSN Coatings Characterization

A M-2000 spectroscopic ellipsometer (J.A. Woollam Co., Lincoln, NE, USA) was used to determine the thickness of the assembled coatings on Si substrates. Data analysis was done using the CompleteEASE software package (version 653). Measurements were performed at wavelengths from 400 to 1000 nm and at angles 45°, 55° and 65°. The data

obtained were fitted using the grade layer Cauchy model, which assumes that the real part of the refractive index (*n*) can be described as follows:

$$n(\lambda) = A + \frac{B}{\lambda^2} + \frac{C}{\lambda^4} \tag{1}$$

where *A*, *B* and *C* are constants and λ is the wavelength of the incident light. The index of refraction was determined as reported as *n* (λ) = *A* due to the negligible contributions of the *B* and *C* terms in the above equation.

The coverage and the maximum topographical thickness of MSN coatings were measured using top-view and cross-sectional scanning electron microscopy (SEM) images, respectively, collected by a JSM-7500F (JEOL USA Inc., Peabody, MA, USA) instrument. For cross-sectional SEM imaging, the wafers were cut using a diamond pen. The images were taken using an accelerating voltage of 5 kV and emission current of 10 μA. The working distance was 12 and 15 mm for top-view and cross-sectional SEM imaging, respectively. Prior to imaging, samples were sputtered with 3 nm Pt/Pd coating to minimize charging and to obtain better quality images. Coverage and cross-sectional thickness analyses were done using the ImageJ software for 10 images per deposition condition.

2.3. Molecular Dynamics (MD)/Density Functional Theory (DFT) Simulations of Ethanol and Methane Adsorption on the Surface of MSNs

First-principles density functional theory (DFT) [36,37] calculations of the surface adhesion were carried out using the Vienna ab initio simulation package (VASP version 5) [38,39]. All the DFT calculations employed the Perdew–Burke–Ernzerhof (PBE) [40] exchange-correlation functional within the generalized gradient approximation. All structural relaxations were performed until atomic force convergence of 0.02 eV/Å and total energy convergence of 1×10^{-6} eV/Å were reached. The plane-wave cutoff was set to 520 eV with a Γ-centered k-points grid of $1 \times 1 \times 1$ due to the large supercell of the slab model used in the calculations. Dipole correction was included to remove the artificial interactions from the periodic images due to the periodic boundary condition in the plane-wave DFT calculations [41,42].

An amorphous SiO_2 (a-SiO_2) slab was constructed using a combination of molecular dynamics (MD) and DFT following a similar method as described by Ewing et al. [43]. First, a cubic FCC SiO_2 structure consisting of 96 atoms was heated to 5000 K and equilibrated for 500 ps, and then rapidly cooled to 300 K at a rate of −0.47 K/ps and held for 100 ps using the large-scale atomic/molecular massively parallel simulator (LAMMPS) [44] and Tersoff interatomic potential [45]. The rapidly cooled a-SiO_2 structure was further relaxed using DFT, and a surface slab was then created by removing atoms at the top/bottom of the cell and adding a vacuum layer of 15 Å along the surface normal with the slab centered in the unit cell. O and H atoms were then added to the unsaturated Si and O atoms on the surface to functionalize the surface with silanol (Si–OH) groups. The functionalized slab was further relaxed to yield a-SiO_2 surface by relaxing the top SiO_2 layer of 5.5 Å near the functionalized surface and fixing the bottom SiO_2 layer of 5.5 Å. To identify potential binding sites on the a-SiO_2 surface, the adsorbent molecule was systematically placed at different initial positions over the surface with the system subsequently relaxed to allow the molecule to migrate to low energy binding sites. The system with the lowest energy was used for the subsequent adsorption energy calculations.

2.4. Detection of Ethanol Vapor and Methane Gas Using Functionalized Amorphous Silicon (a-Si) Waveguides

The a-Si ridge waveguides were fabricated using a complementary metal-oxide-semiconductor (CMOS) compatible process. The images of the a-Si waveguides were acquired by a Tescan FERA-3 model SEM (Brno-Kohoutovice, Czech Republic). The images were taken using an accelerating voltage of 10 kV and a working distance of 9 mm. The dimensions of the a-Si waveguides were 10 μm in width and 1 μm in height. Smooth

2.4. Detection of Ethanol Vapor and Methane Gas Using Functionalized Amorphous Silicon (a-Si) Waveguides

The a-Si ridge waveguides were fabricated using a complementary metal-oxide-semiconductor (CMOS) compatible process. The images of the a-Si waveguides were acquired by a Tescan FERA-3 model SEM (Brno-Kohoutovice, Czech Republic). The images were taken using an accelerating voltage of 10 kV and a working distance of 9 mm. The dimensions of the a-Si waveguides were 10 μm in width and 1 μm in height. Smooth edges of the waveguide were achieved leading to a low optical loss of 2 dB/cm (Figure 1A). The mid-IR system used for gas measurements is shown in Figure 1B. The mid-IR light source was a tunable mid-IR laser (M Squared Firefly, Glasgow, UK) with 150 kHz pulse repetition rate, 10 ns pulse duration, 150 mW average power and a tuning range of 2.5–3.7 μm. Light from the laser was butt-coupled into the a-Si waveguide through a ZrF$_4$ fiber. Fine alignment of the fiber position relative to the waveguide was performed under an optical microscope (OM). At the waveguide output end, another ZrF$_4$ fiber with an 80 μm core diameter was used to collect and deliver the light signal from the waveguide to a photodetector (Thorlabs PDA20H, Newton, NJ, USA). The light intensity obtained by the photodetector was digitized using a multimeter, and the real-time gas measurement results were recorded by a computer. Three types of gases or vapor were used for the gas measurements: nitrogen gas, methane gas and ethanol vapors. Since nitrogen gas is transparent in the mid-IR region, it was used to purge the polydimethylsiloxane (PDMS) chamber between cycles of pure methane gas and ethanol vapors. Ethanol vapors were generated by bubbling nitrogen gas through liquid ethanol at ambient temperature, resulting in a saturated ethanol vapor of concentration of 0.15 g/L. Three mass flow controllers (MFCs) were used to regulate the gas flow rates for these gas lines.
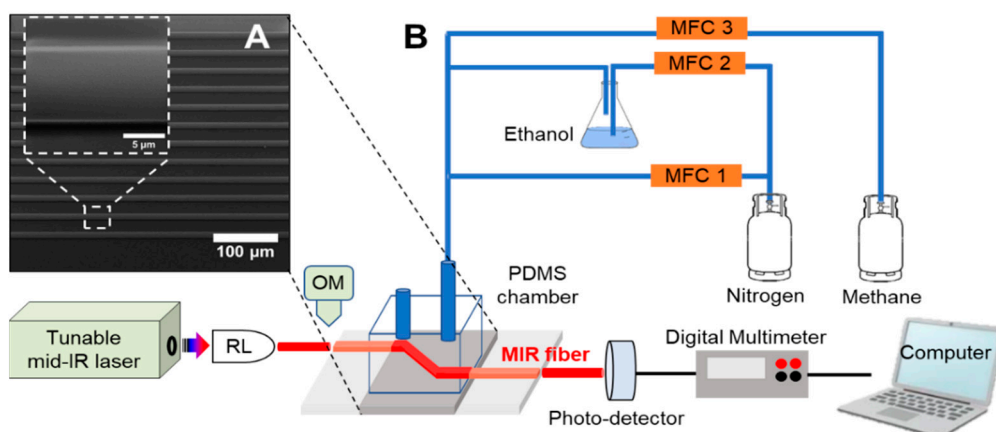

Figure 1. Top-view SEM image of waveguides (WGs) (**A**) and schematic illustrating gas measurement setup (**B**).

3. Results and Discussion

3.1. Synthesized MSNs

Figure 2A shows the TEM images of the synthesized MSNs using the modified Stöber method. Analysis of the TEM images yielded a unimodal distribution of particle sizes with an average diameter of 159 ± 32 nm. MSNs were easily dispersed in water, and measurements with these dispersions at pH 9 using DLS yielded a hydrodynamic diameter of 257 ± 52 nm (Supplementary Materials Figure S1). The negative value of the measured zeta potential of MSNs at pH 9 of −35.6 ± 7.3 mV is consistent with the dissociation of the silanol groups giving rise to a negative charge at the MSN surface. Supplementary Materials Table S1 also shows that similar values of the hydrodynamic diameter and zeta potential were recorded at lower pH values of 7 and 8, which agrees with a low value of isoelectric point of silanol groups (IEP = 2–3 [46]). XRD analysis indicated an absence of sharp peaks in the diffractograms, suggesting purely amorphous structure of MSNs (Supplementary Materials Figure S2). Finally, the most important characteristics of MSNs exploited in this study—the large surface area and porosity of MSNs—were determined using the BET method [35]. These measurements yielded a surface area of 1103.81 m^2/g with a pore size diameter of 2.4 nm calculated using the BJH model. Supplementary Materials Figure S3 presents an adsorption isotherm of nitrogen on the surface of MSNs as a reference.

in the diffractograms, suggesting purely amorphous structure of MSNs (Supplementary Materials Figure S2). Finally, the most important characteristics of MSNs exploited in this study—the large surface area and porosity of MSNs—were determined using the BET method [35]. These measurements yielded a surface area of 1103.81 m^2/g with a pore size diameter of 2.4 nm calculated using the BJH model. Supplementary Materials Figure S3 presents an adsorption isotherm of nitrogen on the surface of MSNs as a reference.
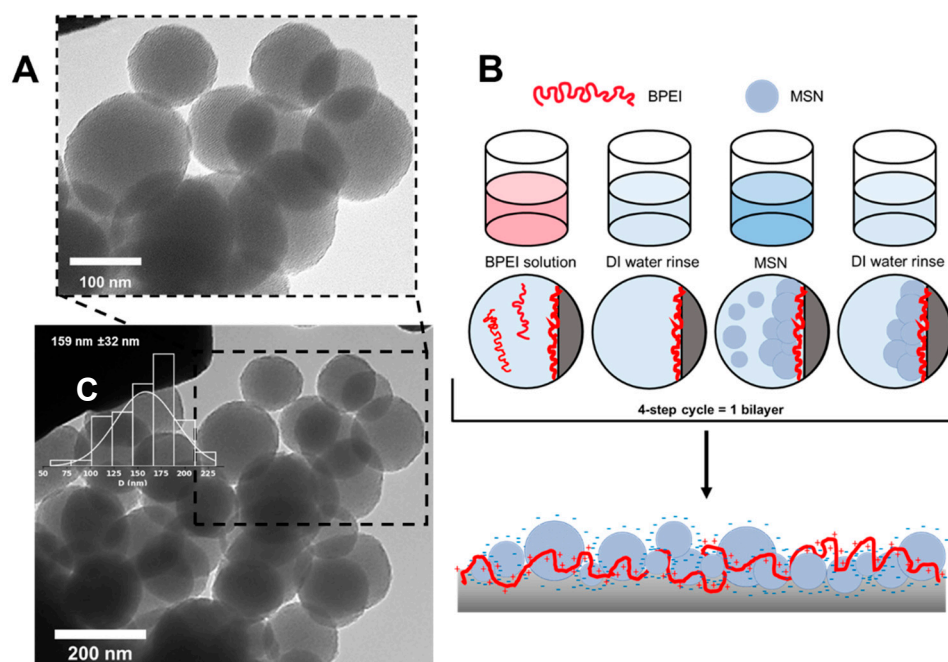
Figure 2. Transmission scanning microscopy (TEM) images for MSNs (**A**) and schematic illustration of deposition of a 1-BL coating using the layer-by-layer (LbL) technique (**B**). The histogram graph within the TEM image was generated via analyzing 200 nanoparticles in several TEM images using imageJ software (**C**).

3.2. BPEI/MSN Coating Assembly

Synthesized MSNs were deposited at three pH values (7, 8 and 9) and using four speeds (0.001, 0.01, 0.1 and 1 cm/s) on the surface of Si wafers within single bilayer using the LbL method as depicted in Figure 2B. Coatings deposited at speeds 0.01, 0.1 and 1 cm/s showed poor visible coverage and poor uniformity. Substrate withdrawal speeds >0.01 cm/s, typically fall in the advective regime where "draining" or gravity forces dominate [47], deteriorating the homogeneity of these coatings. The relatively large, rigid and spherical MSNs seem to "wash-out" as the substrate is pulled out from the solution, which results in the gradient and faded coatings shown in Supplementary Materials Figure S4A–C. On the other hand, substrate withdrawal speeds <0.01 cm/s, usually fall in the convective regime, where capillary forces dominate [48–50], enabling coating homogeneity (Supplementary Materials Figure S4D). In this regime, deposition of MSNs is not controlled by the gravity, but rather supported via capillary forces as the substrate moves upward. Conventional dipping also resulted in uniform, but thinner, visible coatings similar to those deposited at 0.001 cm/s. Thus, coating characterization was performed here mainly for the optimized speed (0.001 cm/s) and conventional deposition used for comparison.

Deposition pH of the priming BPEI and MSN layers significantly affected nanoparticle surface coverage. Supplementary Materials Table S2 shows dry thicknesses for BPEI priming layer deposited at different pH and different substrate withdrawal conditions. The dry thickness of the BPEI layer was only a few nanometers thick, but its thickness was strongly pH dependent, with a higher amount of BPEI deposited at pH 9. At this basic pH, BPEI becomes less positively charged and adopts more "loopy" conformations. The loopiness of the BPEI priming layer provides more surface area for negatively charged MSNs to "stick" [51–53]. As a result, ellipsometric thickness measured after deposition also increased with pH (Supplementary Materials Figure S5). The largest amount of MSN was deposited at pH 9 using controlled dipping at 0.001 cm/s when the BPEI layer was the thickest (3.6 nm vs. 1.0 nm for conventional dipping at the same pH). Supplementary Materials Figure S6 schematically shows how the deposition pH of the precursor layer

loopiness of the BPEI priming layer provides more surface area for negatively charged MSNs to "stick" [51–53]. As a result, ellipsometric thickness measured after deposition also increased with pH (Supplementary Materials Figure S5). The largest amount of MSN was deposited at pH 9 using controlled dipping at 0.001 cm/s when the BPEI layer was the thickest (3.6 nm vs. 1.0 nm for conventional dipping at the same pH). Supplementary Materials Figure S6 schematically shows how the deposition pH of the precursor layer controls the surface coverage of MSNs. Fitted ellipsometric refractive index reported for these 1-BL films is 1.2, which reflects the porosity of these particles compared to solid silica particles of refractive index of 1.46 in the 400–1000 nm range [54].

To directly visualize surface coverage with MSNs, top-view SEM imaging was performed (Figure 3A–D). 1-BL coatings deposited at pH 9 and 0.001 cm/s substrate withdrawal speed resulted in the highest MSN coverage of 40%, which compares favorably relative to the 30% and 28% coverage achieved with coatings deposited at pH 8 and pH 7, respectively. As a reference, conventional dipping resulted in lower coverages: 18%, 14% and 9% for pH 9, 8 and 7, respectively. Supplementary Materials Figure S7 shows that without the BPEI priming layer, negatively charged, bulky MSNs cannot be deposited on bare Si substrates covered with a native oxide layer, since this makes these surfaces negatively charged.
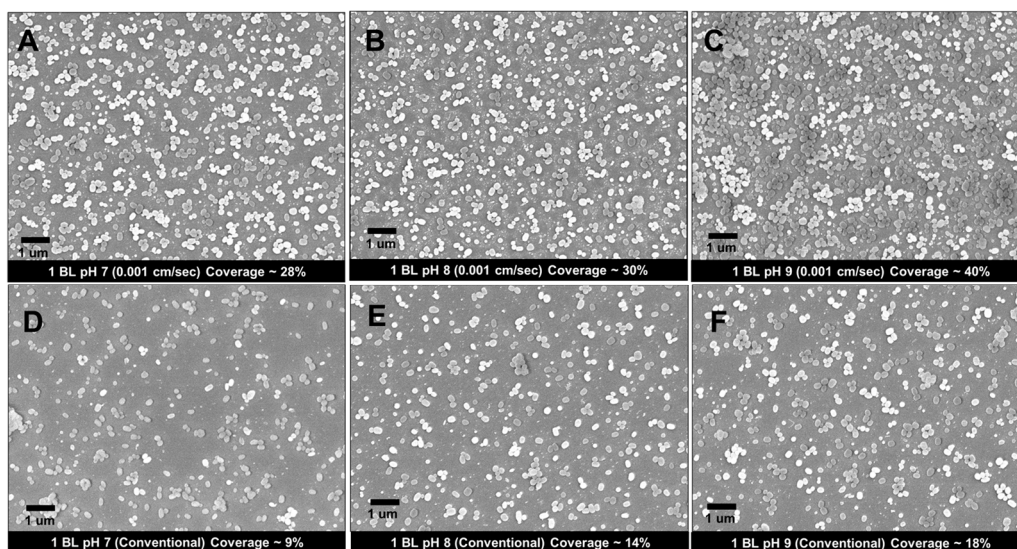

Figure 3. Top-view SEM images of 1-BL coatings deposited at different pH and dipping conditions. The coverage was estimated by ImageJ analysis of 10 images: (**A**): 1-BL coating at pH 7 (controlled dipping at speed 0.001 cm/s); (**B**): 1-BL coating at pH 8 (controlled dipping at speed 0.001 cm/s); (**C**): 1-BL coating at pH 9 (controlled dipping at speed 0.001 cm/s); (**D**): 1-BL coating at pH 7 (conventional dipping); (**E**): 1-BL coating at pH 8 (conventional dipping); (**F**): 1-BL coating at pH 9 (conventional dipping).

Note that the LbL technique can be used to further increase the amount of surface-immobilized MSNs, and surfaces were completely covered by MSNs after five deposition cycles, with more robust coatings produced through controlled deposition (Supplementary Materials Figure S8A) relative to conventional dipping (Supplementary Materials Figure S8B). Further, ellipsometry shows a linear growth for both conventional and controlled dipping deposition at optimum pH 9 (Supplementary Materials Figure S9A). Cross-sectional SEM imaging also indicated that 5-BL coatings were the thickest when controlled rather than when conventional dipping was used (film thicknesses 498 ± 26 nm and 276 ± 40 nm, respectively) even though the 1-BL coatings were similar in thickness (Supplementary Materials Figure S9B–E). This result suggests that for higher number of bilayers, capillary forces seem to further aid deposition of the MSN within these coatings.

3.3. MD/DFT Simulation of Adsorption of Ethanol and Methane Gas at the Surface of MSNs

To explore the ability of surface-immobilized MSNs to selectively adsorb polar and nonpolar gas molecules, theoretical simulations were performed to guide selection of analyte molecules followed by experimental measurements. These simulations were performed for ethanol as a representative polar molecule, and methane as a representative nonpolar gas molecule. Specifically, the adsorption energy (E_{ads}) for ethanol and methane

3.3. MD/DFT Simulation of Adsorption of Ethanol and Methane Gas at the Surface of MSNs

To explore the ability of surface-immobilized MSNs to selectively adsorb polar and nonpolar gas molecules, theoretical simulations were performed to guide selection of analyte molecules followed by experimental measurements. These simulations were performed for ethanol as a representative polar molecule, and methane as a representative nonpolar gas molecule. Specifically, the adsorption energy (E_{ads}) for ethanol and methane molecule was explored using DFT calculations. The adsorption energy can be calculated as $E_{ads} = E_{slab \, + \, molecule} - E_{slab} - E_{molecule}$, where $E_{slab \, + \, molecule}$, E_{slab} and $E_{molecule}$ are the total energy for the system containing both the slab and the adsorbent molecule, the total energy for the slab only and the total energy for isolated ethane or methane molecule only. Supplementary Materials Table S3 shows the calculated total energy and adsorption energy with and without dipole correction, and the effect of dipole correction on the total energy was found to be relatively small. Simulated configurations of ethanol and methane with the a-SiO$_2$ surface are illustrated in Figure 4. Our results predicted a strong binding energy of 662.6 meV for the polar gas, suggesting that there is strong binding between ethanol and the SiO$_2$ surface. Surface silanol groups commonly hydrogen bonds with polar organic vapors [55–57]. In our case, the three binding site were determined to be located between the silanol groups forming strong adhesion via hydrogen bonding. Three SiOH$^{\delta-}$···O$^{\delta-}$H bonds were identified between the surface silanol groups and the alcohol with bond lengths of 1.775, 1.783 and 1.828 Å. In contrast, methane is non-polar with the calculated binding energy of ~43.6 meV, suggesting very weak binding of this analyte with the SiO$_2$ surface.
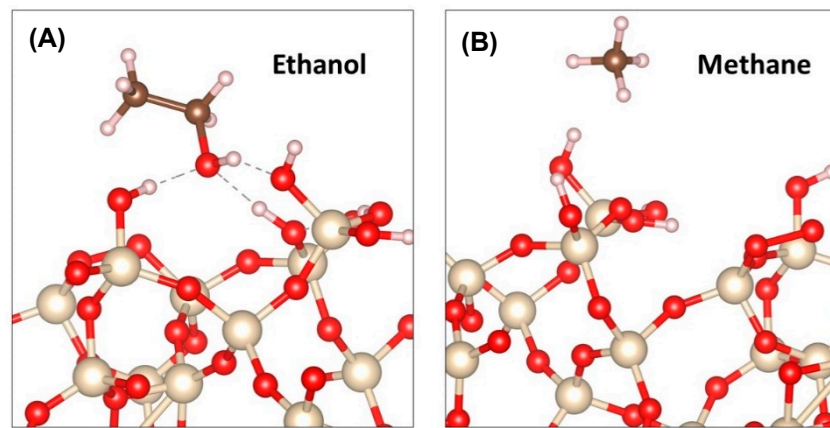

Figure 4. Preferential configuration of (**A**) ethanol and (**B**) methane molecules adsorbed on the surface of amorphous SiO$_2$ nanoparticle.

3.4. Detection of Ethanol Vapor and Methane Gas Using Functionalized a-Si Waveguides

Figure 5A,B illustrates how the WG coated with a monolayer of MSN particles (i.e., obtained by calcination of a 1-BL BPEI/MSN film) was used for on-chip ethanol and methane gas detection. Each analyte was measured at its maximum absorbance peak caused by the C–H stretching vibrations using the setup described in Section 2.4. The corresponding maxima for C–H vibrations occurred at 3320 nm for methane gas and 3350 nm for ethanol vapors. In addition, cross measurements were performed. As depicted in Figure 5C, the largest enhancement occurred at 3350 nm for ethanol, where the absorbance calculated using Beer's law increased from 0.0537 ± 0.001 for bare a-Si waveguide to 0.0802 ± 0.005 for the waveguide coated with MSNs, yielding a 15-fold enhancement in absorbance. In contrast, absorbance changes from the uncoated compared to the coated waveguide for methane gas at 3350 nm was negligible. At methane absorption maximum of 3320 nm, absorption of ethanol was lower, and increased 6-fold, from 0.005 ± 0.002 with a bare a-Si WG to 0.0331 ± 0.007 with the coated WG. Additionally, at 3320 nm the methane absorption was low (0.0107 ± 0.001) for the bare WG, and showed a modest 2-fold increase to 0.0189 ± 0.005 with the coating. These results suggest that our polar MSN surfaces were more efficient in concentrating polar compounds (ethanol) versus non-polar compounds (methane) but did enhance the sensitivity of both gases relative to the bare waveguide at their absorption wavelength maximums. In comparison to our prior work [20], MSNs surpasses the performance of spherical solid nanoparticles utilized for polar vapors (such as acetone) in terms of stability of the measurements and enhancement factor. This can

absorption was low (0.0107 ± 0.001) for the bare WG, and showed a modest 2-fold increase to 0.0189 ± 0.005 with the coating. These results suggest that our polar MSN surfaces were more efficient in concentrating polar compounds (ethanol) versus non-polar compounds (methane) but did enhance the sensitivity of both gases relative to the bare waveguide at their absorption wavelength maximums. In comparison to our prior work [20], MSNs surpasses the performance of spherical solid nanoparticles utilized for polar vapors (such as acetone) in terms of stability of the measurements and enhancement factor. This can be explained by the fact that MSNs are characterized with high porosity, which enhances polar gas adsorption to the surface. Either results Figure 5D also shows that gas adsorption by surface-immobilized MSNs was fully reversible, and multiple cycles of analyte adsorption and desorption could be performed at their optimum absorbance wavelengths within maximum measurement error of ±0.005. These experiments suggest reversible adsorption (i.e., physisorption) of these analytes to the MSN surfaces. Therefore, the experimental results strongly agree with the DFT calculations, which suggest preferential and relatively strong binding between silanol and alcohol groups in comparison to very weak binding silanol groups and methane. Although the LbL technique allowed further increase in the MSNs within the coatings, functionalization with a monolayer of MSNs was sufficient to enhance the performance of our on-chip WG-based sensor while reducing any potential optical losses and interferences from the coating.
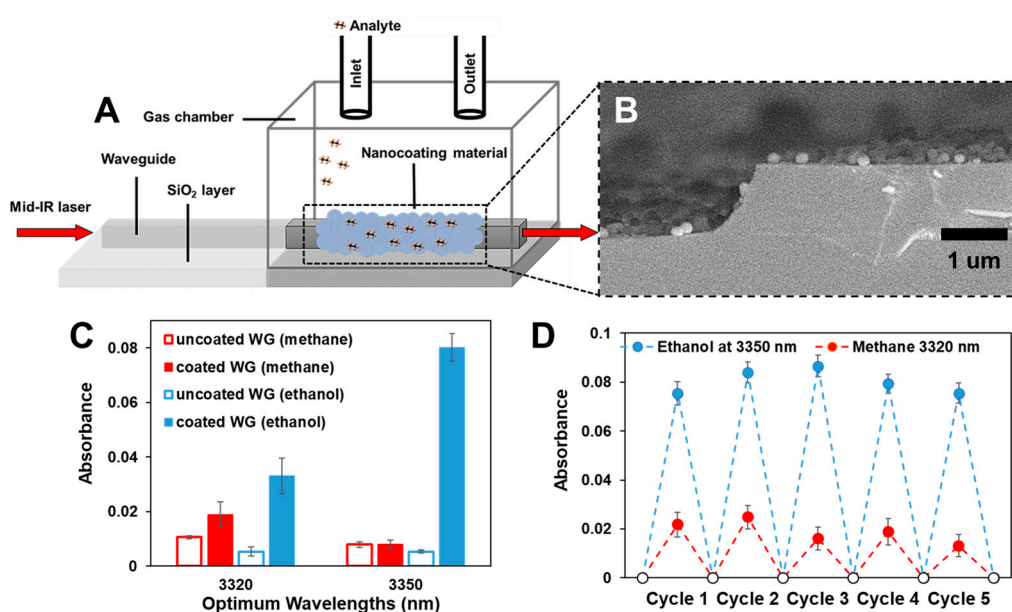

Figure 5. Schematic representation of an optical waveguide sensor (**A**); cross-sectional SEM image of functionalized waveguide with calcinated 1-BL film (**B**); graph showing absorbance of ethanol and methane for 1-BL film coated and uncoated WGs at their optimum wavelengths 3350 and 3320 nm, respectively (**C**) and graph showing reversibility measurements of ethanol and methane at their optimum wavelengths (**D**).

4. Conclusions

This work has shown the potential of surface functionalization of MIR WGs with MSNs using the LbL technique to enhance sensitivity and selectivity for the detection of VOCs. Deposition of robust conformal coatings of porous nanoparticles was enabled by the precise control of polymer precursor and MSN deposition conditions, including solution pH and substrate withdrawal speed.

Figure S9: Comparison of controlled and conventional dipping ellipsometric thickness as a function of number of bilayers (A). and cross-sectional SEM images of 1- and 5-BL films at pH 9 (B-E): 1-BL film at 0.001 cm/s (B); 5-BL film at 0.001 cm/s (C); 1-BL film using conventional dipping (D); and 5-BL film using conventional dipping (E). Refractive indices of these films were fitted accordingly. Cross-sectional SEM thicknesses were estimated using ImageJ software analysis of 10 images collected from samples prepared by using several repeated coating depositions, Table S1: Zeta potentials and hydrodynamic diameters for MSN 0.2 wt.% aqueous solutions at pH 7 and 8, Table S2: Dry ellipsometric thickness of a BPEI priming layer as a function of solution pH and substrate withdrawal conditions, Table S3: Total energy and adsorption energy of ethanol and methane molecule on a-SiO_2 surface with and without dipole correction.

Author Contributions: Conceptualization, D.A.H., Y.K., and S.A.S.; methodology, D.A.H., Y.K., and S.A.S.; validation, D.A.H., Y.K., J.Z., and D.W.; formal analysis, D.A.H., Y.K., J.Z., D.W., X.Q., R.G.-O., G.L.C., P.T.L., and S.A.S.; investigation, D.A.H., Y.K., J.Z., D.W., X.Q., R.G.-O., G.L.C., P.T.L., and S.A.S.; resources, X.Q., R.G.-O., G.L.C., P.T.L., and S.A.S.; data curation, D.A.H., Y.K., J.Z., D.W., X.Q., R.G.-O., G.L.C., P.T.L., and S.A.S.; writing—original draft preparation, D.A.H. and S.A.S.; writing—review and editing, D.A.H., Y.K., J.Z., D.W., X.Q., R.G.-O., G.L.C., P.T.L., and S.A.S.; visualization, D.A.H. and S.A.S.; supervision, X.Q., D.A.H., R.G.-O., G.L.C., P.T.L., and S.A.S.; project administration, D.A.H., R.G.-O., G.L.C., P.T.L., and S.A.S.; funding acquisition, X.Q., R.G.-O., G.L.C., P.T.L., and S.A.S. All authors have read and agreed to the published version of the manuscript.

Institutional Review Board Statement: Not applicable.

Informed Consent Statement: Not applicable.

Data Availability Statement: The data presented in this study are available on request from the corresponding author. The data are not publicly available due to privacy.

Conflicts of Interest: The authors declare no conflict of interest.

References

1. Henderson, B.; Khodabakhsh, A.; Metsälä, M.; Ventrillard, I.; Schmidt, F.M.; Romanini, D.; Ritchie, G.A.; te Lintel Hekkert, S.; Briot, R.; Risby, T.; et al. Laser spectroscopy for breath analysis: Towards clinical implementation. *Appl. Phys. B* **2018**, *124*, 161. [CrossRef] [PubMed]
2. Selvaraj, R.; Vasa, N.J.; Nagendra, S.M.S.; Mizaikoff, B. Advances in mid-infrared spectroscopy-based sensing techniques for exhaled breath diagnostics. *Molecules* **2020**, *25*, 2227. [CrossRef]
3. Lamote, K.; Brinkman, P.; Vandermeersch, L.; Vynck, M.; Sterk, P.J.; van Langenhove, H.; Thas, O.; van Cleemput, J.; Nackaerts, K.; van Meerbeeck, J.P. Breath analysis by gas chromatography-mass spectrometry and electronic nose to screen for pleural mesothelioma: A cross-sectional case-control stud. *Oncotarget* **2017**, *8*, 91593–91602. [CrossRef] [PubMed]
4. Wang, X.R.; Cassells, J.; Berna, A.Z. Stability control for breath analysis using GC-MS. *J. Chromatogr. B* **2018**, *1097*, 27–34. [CrossRef] [PubMed]
5. Masikini, M.; Chowdhury, M.; Nemraoui, O. Review—Metal oxides: Application in exhaled breath acetone chemiresistive sensors. *J. Electrochem. Soc.* **2020**, *167*, 037537. [CrossRef]
6. Paul, R.K.; Badhulika, S.; Saucedo, N.M.; Mulchandani, A. Graphene nanomesh as highly sensitive chemiresistor gas sensor. *Anal. Chem.* **2012**, *84*, 8171–8178. [CrossRef]
7. Righettoni, M.; Amann, A.; Pratsinis, S.E. Breath analysis by nanostructured metal oxides as chemo-resistive gas sensors. *Mater. Today* **2015**, *18*, 163–171. [CrossRef]
8. Park, C.O.; Fergus, J.W.; Miura, N.; Park, J.; Choi, A. Solid-state electrochemical gas sensors. *Ionics* **2009**, *15*, 261–284. [CrossRef]
9. Schädle, T.; Mizaikoff, B. Mid-infrared waveguides: A perspective. *Appl. Spectrosc.* **2016**, *70*, 1625–1638. [CrossRef]
10. Wu, J.; Yue, G.; Chen, W.; Xing, Z.; Wang, J.; Wong, W.R.; Cheng, Z.; Set, S.Y.; Murugan, G.S.; Wang, X.; et al. On-chip optical gas sensors based on group-IV materials. *ACS Photonics* **2020**, *7*, 2923–2940. [CrossRef]

11. Jin, T.N.; Zhou, J.C.; Lin, P.T. Real-time and non-destructive hydrocarbon gas sensing using mid-infrared integrated photonic circuits. *RSC Adv.* **2020**, *10*, 7452–7459. [CrossRef] [PubMed]

12. Messica, A.; Greenstein, A.; Katzir, A. Theory of fiber-optic, evanescent-wave spectroscopy andsensors. *Appl. Opt.* **1996**, *35*, 2274–2284. [CrossRef] [PubMed]

13. Pandraud, G.; Koster, T.M.; Gui, C.; Dijkstra, M.; van den Berg, A.; Lambeck, P.V. Evanescent wave sensing: New features for detection in small volumes. *Sens. Actuators A Phys.* **2000**, *85*, 158–162. [CrossRef]

14. Giammarco, J.; Zdyrko, B.; Petit, L.; Musgraves, J.D.; Hu, J.; Agarwal, A.; Kimerling, L.; Richardson, K.; Luzinov, I. Towards universal enrichment nanocoating for IR-ATR waveguides. *Chem. Commun.* **2011**, *47*, 9104–9106. [CrossRef] [PubMed]

15. Pejcic, B.; Boyd, L.; Myers, M.; Ross, A.; Raichlin, Y.; Katzir, A.; Lu, R.; Mizaikoff, B. Direct quantification of aromatic hydrocarbons in geochemical fluids with a mid-infrared attenuated total reflection sensor. *Org. Geochem.* **2013**, *55*, 63–71. [CrossRef]

16. Schädle, T.; Pejcic, B.; Myers, M.; Mizaikoff, B. Fingerprinting oils in water via their dissolved VOC pattern using mid-infrared sensors. *Anal. Chem.* **2014**, *86*, 9512–9517. [CrossRef]

17. Stach, R.; Pejcic, B.; Crooke, E.; Myers, M.; Mizaikoff, B. Mid-infrared spectroscopic method for the identification and quantification of dissolved oil components in marine environments. *Anal. Chem.* **2015**, *87*, 12306–12312. [CrossRef]

18. Miller, D.D.; Chuang, S.S.C. Control of CO_2 Adsorption and desorption using polyethylene glycol in a tetraethylenepentamine thin film: An in situ ATR and theoretical study. *J. Phys. Chem. C* **2016**, *120*, 25489–25504. [CrossRef]

19. Wilfong, W.C.; Srikanth, C.S.; Chuang, S.S.C. In situ ATR and DRIFTS studies of the nature of adsorbed CO_2 on tetraethylenepentamine films. *ACS Appl. Mater. Interfaces* **2014**, *6*, 13617–13626. [CrossRef]

20. Al Husseini, D.; Zhou, J.; Willhelm, D.; Hastings, T.; Day, G.S.; Zhou, H.-C.; Coté, G.L.; Qian, X.; Gutierrez-Osuna, R.; Lin, P.T.; et al. All-nanoparticle layer-by-layer coatings for mid-IR on-chip gas sensing. *Chem. Commun.* **2020**, *56*, 14283–14286. [CrossRef]

21. Satheeshkumar, E.; Yang, J. Preparation and characterization of silver film coated ZnO nanowire gas sensors based on the infrared surface enhancement effect for detection of VOCs. *RSC Adv.* **2014**, *4*, 19331–19337. [CrossRef]

22. Zhuk, A.; Sukhishvili, S.A. Stimuli-responsive layer-by-layer nanocomposites. *Soft Matter* **2013**, *9*, 5149–5154. [CrossRef]

23. Zhang, X.; Xu, Y.; Zhang, X.; Wu, H.; Shen, J.; Chen, R.; Xiong, Y.; Li, J.; Guo, S. Progress on the layer-by-layer assembly of multilayered polymer composites: Strategy, structural control and applications. *Prog. Polym. Sci.* **2019**, *89*, 76–107. [CrossRef]

24. Qiu, H.; Lee, W.Y.; Sukhishvili, S.A. Layer-by-layer self-assembly of ceramic particles for coating complex shape substrates. *J. Am. Ceram. Soc.* **2006**, *89*, 1180–1187. [CrossRef]

25. Palaniappan, A.; Li, X.; Tay, F.E.H.; Li, J.; Su, X. Cyclodextrin functionalized mesoporous silica films on quartz crystal microbalance for enhanced gas sensing. *Sens. Actuators B Chem.* **2006**, *119*, 220–226. [CrossRef]

26. Chang, Y.C.; Bai, H.; Li, S.N.; Kuo, C.N. Bromocresol green/mesoporous silica adsorbent for ammonia gas sensing via an optical sensing instrument. *Sensors* **2011**, *11*, 4060–4072. [CrossRef]

27. Sebők, D.; Janovák, L.; Kovács, D.; Sápi, A.; Dobó, D.G.; Kukovecz, Á.; Kónya, Z.; Dékány, I. Room temperature ethanol sensor with sub-ppm detection limit: Improving the optical response by using mesoporous silica foam. *Sens. Actuators B Chem.* **2017**, *243*, 1205–1213. [CrossRef]

28. Echeverría, J.C.; de Vicente, P.; Estella, J.; Garrido, J.J. A fiber-optic sensor to detect volatile organic compounds based on a porous silica xerogel film. *Talanta* **2012**, *99*, 433–440. [CrossRef]

29. Amonette, J.E.; Matyáš, J. Functionalized silica aerogels for gas-phase purification, sensing, and catalysis: A review. *Microporous Mesoporous Mater.* **2017**, *250*, 100–119. [CrossRef]

30. Han, B.-H.; Manners, I.; Winnik, M.A. Oxygen sensors based on mesoporous silica particles on layer-by-layer self-assembled films. *Chem. Mat.* **2005**, *17*, 3160–3171. [CrossRef]

31. Danan, Y.; Ilovitsh, T.; Ramon, Y.; Malka, D.; Liu, D.; Zalevsky, Z. Silicon-coated gold nanoparticles nanoscopy. *J. Nanophotonics* **2016**, *10*, 036015. [CrossRef]

32. Pinhas, H.; Malka, D.; Danan, Y.; Sinvani, M.; Zalevsky, Z. Design of fiber-integrated tunable thermo-optic C-band filter based on coated silicon slab. *J. Eur. Opt. Soc. Rapid Publ.* **2017**, *13*, 32. [CrossRef]

33. Ioudashkin, E.; Malka, D. A Three demultiplexer C-band using angled multimode interference in GaN–SiO_2 slot waveguide structures. *Nanomaterials* **2020**, *10*, 2338. [CrossRef] [PubMed]

34. Kim, T.-W.; Chung, P.-W.; Lin, V.S.Y. Facile synthesis of monodisperse spherical MCM-48 mesoporous silica nanoparticles with controlled particle size. *Chem. Mat.* **2010**, *22*, 5093–5104. [CrossRef]

35. Brunauer, S.; Emmett, P.H.; Teller, E. Adsorption of gases in multimolecular layers. *J. Am. Chem. Soc.* **1938**, *60*, 309–319. [CrossRef]

36. Hohenberg, P.; Kohn, W. Inhomogeneous electron gas. *Phys. Rev.* **1964**, *136*, B864–B871. [CrossRef]

37. Kohn, W.; Sham, L.J. Self-consistent equations including exchange and correlation effects. *Phys. Rev.* **1965**, *140*, A1133–A1138. [CrossRef]

38. Kresse, G.; Furthmüller, J. Efficiency of ab-initio total energy calculations for metals and semiconductors using a plane-wave basis set. *Comput. Mater. Sci.* **1996**, *6*, 15–50. [CrossRef]

39. Kresse, G.; Furthmüller, J. Efficient iterative schemes for ab initio total-energy calculations using a plane-wave basis set. *Phys. Rev. B* **1996**, *54*, 11169–11186. [CrossRef] [PubMed]

40. Perdew, J.P.; Burke, K.; Ernzerhof, M. Generalized gradient approximation made simple. *Phys. Rev. Lett.* **1996**, *77*, 3865–3868. [CrossRef] [PubMed]

41. Neugebauer, J.; Scheffler, M. Adsorbate-substrate and adsorbate-adsorbate interactions of Na and K adlayers on Al(111). *Phys. Rev. B* **1992**, *46*, 16067–16080. [CrossRef] [PubMed]

42. Bengtsson, L. Dipole correction for surface supercell calculations. *Phys. Rev. B* **1999**, *59*, 12301–12304. [CrossRef]

43. Ewing, C.S.; Bhavsar, S.; Veser, G.; McCarthy, J.J.; Johnson, J.K. Accurate amorphous silica surface models from first-principles thermodynamics of surface dehydroxylation. *Langmuir* **2014**, *30*, 5133–5141. [CrossRef] [PubMed]

44. Plimpton, S. Fast parallel algorithms for short-range molecular dynamics. *J. Comput. Phys.* **1995**, *117*, 1–19. [CrossRef]

45. Munetoh, S.; Motooka, T.; Moriguchi, K.; Shintani, A. Interatomic potential for Si–O systems using Tersoff parameterization. *Comput. Mater. Sci.* **2007**, *39*, 334–339. [CrossRef]

46. Parks, G.A. The isoelectric points of solid oxides, solid hydroxides, and aqueous hydroxo complex systems. *Chem. Rev.* **1965**, *65*, 177–198. [CrossRef]

47. Landau, L.; Levich, B. Dragging of a liquid by a moving plate. *Acta Physicochim. URSS* **1942**, *17*, 42–54.

48. Faustini, M.; Boissiere, C.; Nicole, L.; Grosso, D. From chemical solutions to inorganic nanostructured materials: A journey into evaporation-driven processes. *Chem. Mat.* **2014**, *26*, 709–723. [CrossRef]

49. Faustini, M.; Louis, B.; Albouy, P.A.; Kuemmel, M.; Grosso, D. Preparation of sol−gel films by dip-coating in extreme conditions. *J. Phys. Chem. C* **2010**, *114*, 7637–7645. [CrossRef]

50. Schneller, T.; Waser, R.; Kosec, M.; Payne, D. *Chemical Solution Deposition of Functional Oxide Thin Films*; Springer: Vienna, Austria, 2016; pp. 233–261.

51. Tan, S.; Erol, M.; Sukhishvili, S.; Du, H. Substrates with discretely immobilized silver nanoparticles for ultrasensitive detection of anions in water using surface-enhanced raman scattering. *Langmuir* **2008**, *24*, 4765–4771. [CrossRef]

52. Erol, M.; Du, H.; Sukhishvili, S. Control of specific attachment of proteins by adsorption of polymer layers. *Langmuir* **2006**, *22*, 11329–11336. [CrossRef] [PubMed]

53. Han, Y.; Tan, S.; Oo, M.K.K.; Pristinski, D.; Sukhishvili, S.; Du, H. Towards full-length accumulative surface-enhanced raman scattering-active photonic crystal fibers. *Adv. Mater.* **2010**, *22*, 2647–2651. [CrossRef] [PubMed]

54. Brixner, B. Refractive-index interpolation for fused silica. *J. Opt. Soc. Am.* **1967**, *57*, 674–676. [CrossRef]

55. Penta, N.K.; Peethala, B.C.; Amanapu, H.P.; Melman, A.; Babu, S.V. Role of hydrogen bonding on the adsorption of several amino acids on SiO_2 and Si_3N_4 and selective polishing of these materials using ceria dispersions. *Colloids Surf. A Physicochem. Eng. Asp.* **2013**, *429*, 67–73. [CrossRef]

56. Liu, D.; Ma, G.; Xu, M.; Allen, H.C. Adsorption of ethylene glycol vapor on α-Al_2O_3 (0001) and amorphous SiO_2 surfaces: Observation of molecular orientation and surface hydroxyl groups as sorption sites. *Environ. Sci. Technol.* **2005**, *39*, 206–212. [CrossRef] [PubMed]

57. Meng, M.; Stievano, L.; Lambert, J.F. Adsorption and thermal condensation mechanisms of amino acids on oxide supports. 1. glycine on silica. *Langmuir* **2004**, *20*, 914–923. [CrossRef]